Journal of the Korean Astronomical Society
49: 83 ∼ 92, 2016 June
©2016. The Korean Astronomical Society. All rights reserved.
http://dx.doi.org/10.5303/JKAS.2016.49.3.83
pISSN: 1225-4614 · eISSN: 2288-890X
http://jkas.kas.org

Re-Acceleration Model for the 'Toothbrush' Radio Relic

Hyesung Kang
Department of Earth Sciences, Pusan National University, Geumjeong-gu, Busan 46241, Korea; hskang@pusan.ac.kr

Received March 20, 2016; accepted May 9, 2016

Abstract: The Toothbrush radio relic associated with the merging cluster 1RXS J060303.3 is presumed to be produced by relativistic electrons accelerated at merger-driven shocks. Since the shock Mach number inferred from the observed radio spectral index, $M_{\rm radio} \approx 2.8$, is larger than that estimated from X-ray observations, $M_{\rm X} \lesssim 1.5$, we consider the re-acceleration model in which a weak shock of $M_s \approx 1.2 - 1.5$ sweeps through the intracluster plasma with a preshock population of relativistic electrons. We find the models with a power-law momentum spectrum with the slope, $s \approx 4.6$, and the cutoff Lorentz factor, $\gamma_{e,c} \approx 7 - 8 \times 10^4$ can reproduce reasonably well the observed profiles of radio fluxes and integrated radio spectrum of the head portion of the Toothbrush relic. This study confirms the strong connection between the ubiquitous presence of fossil relativistic plasma originated from AGNs and the shock-acceleration model of radio relics in the intracluster medium.

Key words: acceleration of particles — cosmic rays — galaxies: clusters: general — shock waves

1. Introduction

Some galaxy clusters contain diffuse radio sources on scales as large as ∼2 Mpc called 'radio relics' (e.g., Feretti et al. 2012; Brüggen et al. 2012; Brunetti & Jones 2014). These 'radio relics' can be classified into two main groups based on their origins and properties (Kempner et al. 2004). *AGN relics/Radio phoenix* are thought to originate from AGNs. AGN relics are radio-emitting relativistic plasma left over from jets and lobes of extinct AGNs, which eventually turn into 'radio ghosts' when the electron plasma becomes radio-quiet due to synchrotron and inverse Compton (iC) energy losses (Ensslin 1999). Radio ghosts may be reborn as *radio phoenix*, if cooled electrons with the Lorentz factor $\gamma_e \lesssim 100$ are compressed and re-energized to $\gamma_e \sim 10^4$ by structure formation shocks (Ensslin & Gopal-Krishna 2001). AGN relics/Radio phoenix typically have roundish shapes and steep-curved integrated spectra of aged electron populations, and they are found near their source AGN (e.g., Slee et al. 2001; van Weeren et al. 2011; Clarke et al. 2013; de Gasperin et al. 2015).

Radio gischt relics, on the other hand, are thought to be produced via Fermi first order process at merger-driven shock waves in the intracluster medium (ICM). They show thin elongated morphologies, spectral steepening downstream of the putative shock, integrated radio spectra with a power-law form, and high polarization level (Ensslin et al. 1998; van Weeren et al. 2010). Most of the observed features of radio *gischt* relics can be adequately explained by diffusive shock acceleration (DSA) model in which relativistic electrons are (re-)accelerated at shock waves: (1) gradual spectral steepening across the relic width, (2) power-law-like integrated spectrum with the spectral index that is larger by 0.5 than the spectral index at the relic edge, i.e., $\alpha_{\rm int} \sim \alpha_{\rm sh} + 0.5$, and (3) high polarization level up to 50% that is expected from the shock compression of turbulent magnetic fields (e.g., van Weeren et al. 2010; Brunetti & Jones 2014). Moreover, it is now well accepted from both observational and theoretical studies that the cosmological shocks are ubiquitous in the ICM and nonthermal particles can be accelerated at such shocks via the DSA process (e.g., Ryu et al. 2003; Vazza et al. 2009; Skillman et al. 2011; Hong et al. 2014).

Yet there remain some puzzles in the DSA origin of radio gischt relics such as low acceleration efficiency of weak shocks and low frequency of merging clusters with detected radio relics. The structure formation shocks with high kinetic energy fluxes, especially those induced by cluster mergers, are thought to have small Mach numbers of $M_s \lesssim 3$ (Ryu et al. 2003; Vazza et al. 2009), while the DSA efficiency at such weak shocks is expected to be extremely low (Kang & Ryu 2011). In particular, it is not well understood how seed electrons are injected into the Fermi first order process at weak shocks that form in the high-beta ($\beta = P_{\rm gas}/P_{\rm mag} \sim 100$) ICM plasma (e.g., Kang et al. 2014). Based on structure formation simulations, the mean separation between shock surfaces in the ICM is expected to be about 1 Mpc (Ryu et al. 2003). Then several shocks and associated radio relics could be present in merging clusters, if every shock were to produce relativistic electrons. Yet only ∼ 10% of luminous merging clusters are observed to host radio relics (Feretti et al. 2012). Furthermore, in some clusters a shock is detected in X-ray observations without associated diffuse radio sources (e.g., Russell et al. 2011).

In order to solve these puzzles re-acceleration of fossil electrons pre-existing in the ICM was proposed by several authors (e.g., Kang & Ryu 2011; Kang et al.

Corresponding author: H. Kang

2012; Pinzke et al. 2013). The presence of radio galaxies, AGN relics and radio phoenix implies that the ICM may host radio-quiet ghosts of fossil electrons (Kang & Ryu 2016). In addition, fossil electrons can be produced by previous episodes of shocks and turbulence that are induced by merger-driven activities. Since fossil electrons with $\gamma_e \gtrsim 100$ can provide seed electrons to the DSA process and enhance the acceleration efficiency, they will alleviate the low acceleration efficiency problem of weak ICM shocks. Moreover, the re-acceleration scenario may explain the low occurrence of radio relics among merging clusters, since the ICM shocks can light up as radio relics only when they encounter clouds of fossil electrons (Kang & Ryu 2016).

The giant radio relic found in the merging cluster 1RXS J060303.3, the so-called 'Toothbrush' relic is a typical example of radio gischt relic. It has a peculiar linear morphology with multiple components that look like the head and handle of a toothbrush (van Weeren et al. 2012). Recently, van Weeren et al. (2016) reported that the spectral index at the northern edge of B1 relic (the head portion of the Toothbrush) is $\alpha_{\rm sh} \approx 0.8$ with the corresponding radio Mach number, $M_{\rm radio} \approx 2.8$ (see Equation 1). But the gas density jump around B1 inferred from X-ray observations implies a much weaker shock with $M_{\rm X} \approx 1.2 - 1.5$. This discrepancy between $M_{\rm radio}$ and $M_{\rm X}$ can be explained, assuming a pre-existing population of relativistic electrons with the right power-law slope, i.e., $f_{\rm up}(p) \propto p^{-4.6}$.

In this study, we attempt to explain the observed properties of relic B1 by the re-acceleration model in which a low Mach number shock ($M_s \approx 1.2 - 1.5$) sweeps though a cloud of pre-existing relativistic electrons. In the next section, we explain some basic physics of the DSA model, while numerical simulations and shock models are described in Section 3. Comparison of our results with observations is presented in Section 4. A brief summary is given in Section 5.

2. DSA Model

2.1. Electron and Radiation Spectra of Radio Relics

According to the DSA model for a *steady planar* shock, the electrons that are injected and accelerated at a shock of sonic Mach number M_s form a power-law momentum distribution, $f_e(p, r_s) \propto p^{-q}$ with $q = 4M_s^2/(M_s^2 - 1)$ (Drury 1983). The electron spectrum integrated over the downstream region of the shock then steepens by one power of momentum, i.e., $F_e(p) \propto p^{-(q+1)}$ due to synchrotron and iC cooling (Ensslin et al. 1998).

The radio synchrotron spectrum $j_\nu(r_s)$ at the shock position r_s, then becomes a power-law, i.e., $j_\nu(r_s) \propto \nu^{-\alpha_{\rm sh}}$ with the shock index

$$\alpha_{\rm sh} = \frac{(q-3)}{2} = \frac{(M_s^2+3)}{2(M_s^2-1)}. \quad (1)$$

This relation is often used to infer the Mach number of the putative shock, $M_{\rm radio}$, from the radio spectral index. Moreover, the volume-integrated radio spectrum behind the shock becomes another steepened power-law, $J_\nu \propto \nu^{-\alpha_{\rm int}}$ with the 'integrated' index $\alpha_{\rm int} = \alpha_{\rm sh} + 0.5$ above the break frequency $\nu_{\rm br}$. Note that the break frequency depends on the magnetic field strength, B, and the shock age, $t_{\rm age}$, as follows:

$$\nu_{\rm br} \approx 0.63\,{\rm GHz} \left(\frac{t_{\rm age}}{100{\rm Myr}}\right)^{-2} \left[\frac{(5\ \mu{\rm G})^2}{B^2 + B_{\rm rad}^2}\right]^2 \left(\frac{B}{5\ \mu{\rm G}}\right), \quad (2)$$

where $B_{\rm rad} = 3.24\ \mu{\rm G}(1+z)^2$ and B is expressed in units of μG and z is the redshift (Kang 2011).

However, such expectations for simple power-law spectra need to be modified in real observations. If the break frequency $\nu_{\rm br}$ lies in the range of observation frequencies (typically $0.1 \lesssim \nu_{\rm obs} \lesssim 10$ GHz), for instance, the integrated radio spectrum steepens gradually over $\sim (0.1 - 10)\nu_{\rm br}$, instead of forming a single power-law (Kang 2015a). Furthermore, in the case of spherically expanding shocks with varying speeds, both the electron spectrum and the ensuing radio spectrum exhibit spectral curvatures (Kang 2015b). In fact, spectral steepening above ~ 2 GHz has been detected in the relic in A2256 (Trasatti et al. 2015) and in the Sausage relic in CIZA J2242.8+5301 (Stroe et al. 2016). The integrated spectral index of B1 of the Toothbrush relic increases from $\alpha_{\rm int} \approx 1.0$ below 2.5 GHz to $\alpha_{\rm int} \approx 1.4$ above 2.0 GHz (Stroe et al. 2016).

In the re-acceleration model, on the other hand, the re-accelerated electron spectrum will depend on the shape of the initial spectrum of pre-existing electrons (e.g., Kang & Ryu 2015). For the preshock electron population of a power-law form, $f_{\rm up} \propto p^{-s}$, for example, the ensuing radio spectrum at the shock position can have $\alpha_{\rm sh} \le (s-3)/2$ or $\alpha_{\rm sh} \le (q-3)/2$, depending on s, q, and observation frequencies (Kang & Ryu 2016). Hence, in the re-acceleration model, the Mach number of the putative shock cannot be inferred directly from the radio spectral index, based on the expectation of the simple version of DSA model. This may explain the fact that in some radio relics such as the Toothbrush relic, the radio Mach number, $M_{\rm radio}$, estimated from the radio spectral index does not agree with the X-ray Mach number, $M_{\rm X}$, estimated from the discontinuities in X-ray observations (e.g., Akamatsu & Kawahara 2013)

2.2. Width of Radio Relics

The cluster RX J0603.3+4214 that hosts the Toothbrush relic is located at the redshift $z = 0.225$ (van Weeren et al. 2012). The recent observations of van Weeren et al. (2016) show that FWHMs of B1 relic at 150 MHz and 610 MHz are about 140 kpc and 110 kpc, respectively, and the spectral index between these two frequencies, $\alpha_{0.15}^{0.61}$, increases from 0.8 at the northern edge of B1 to 1.9 at ~ 200 kpc toward the cluster center. The width of B1 relic at 610 MHz is about 2 times larger than the FWHM ~ 55 kpc of the Sausage relic at 630 MHz (van Weeren et al. 2010).

In the postshock region, accelerated electrons lose energy via synchrotron emission and iC scattering off the

cosmic background radiation over the time scale:

$$t_{\rm rad}(\gamma_e) = 9.8\times 10^7 \text{ yr}\left[\frac{(5\ \mu\text{G})^2}{B^2+B_{\rm rad}^2}\right]^2\left(\frac{\gamma_e}{10^4}\right)^{-1} \quad (3)$$

(Kang 2011). For low energy electrons, the physical width of the postshock volume of radio-emitting electrons is simply determined by the advection length, $\Delta l_{\rm adv} \approx u_2 \cdot t_{\rm age}$, where u_2 is the downstream flow speed. For high energy electrons, on the other hand, it becomes the cooling length, $\Delta l_{\rm cool}(\gamma_e) \approx u_2 \cdot t_{\rm rad}(\gamma_e)$. So the width of the radio-emitting shell of electrons with γ_e is $\Delta l(\gamma_e) = \min[\Delta l_{\rm cool}(\gamma_e), \Delta l_{\rm adv}]$.

In order to connect the spatial distribution of electrons with that of radio emission, one can use the fact that the synchrotron emission from mono-energetic electrons with $\gamma_{\rm e}$ peaks around

$$\nu_{\rm peak} \approx 0.63 \text{ GHz}\cdot\left(\frac{B}{5\ \mu\text{G}}\right)\left(\frac{\gamma_e}{10^4}\right)^2, \quad (4)$$

along with the relation between the observation frequency and the source frequency, $\nu_{\rm obs} = \nu_{\rm peak}/(1+z)$. For low frequency radio emission emitted by uncooled, low energy electrons, the width of radio relics becomes similar to the advection length:

$$\Delta l_{\rm low} \approx 100 \text{ kpc}\cdot u_{2,3}\cdot\left(\frac{t_{\rm age}}{100 \text{ Myr}}\right), \quad (5)$$

where $u_{2,3} = u_2/10^3$ km s^{-1}.

For high frequency emission radiated by cooled high energy electrons, the relic width would be similar to the cooling length (Kang & Ryu 2015):

$$\Delta l_{\rm high} \approx 100 \text{ kpc}\cdot W\cdot u_{2,3}\cdot Q\cdot\left[\frac{\nu_{\rm obs}(1+z)}{0.63\text{GHz}}\right]^{-1/2}. \quad (6)$$

Here the factor $W \sim 1.2-1.3$ takes account for the fact that the spatial distribution of synchrotron emission at $\nu_{\rm peak}$ is somewhat broader than that of electrons with the corresponding γ_e, because more abundant, lower energy electrons also make contributions (Kang 2015a). The factor Q is defined as

$$Q(B,z) \equiv \left[\frac{(5\ \mu\text{G})^2}{B^2+B_{\rm rad}(z)^2}\right]\left(\frac{B}{5\ \mu\text{G}}\right)^{1/2}, \quad (7)$$

where again B and $B_{\rm rad}$ must be expressed in units of microgauss. Figure 1 shows that Q evaluated for $z = 0.225$ peaks at $B \approx 2.8\ \mu$G. Note that for a given value Q there are two possible values of B that satisfy Equation (7).

For B1 relic in the Toothbrush cluster, the estimated downstream speed is $u_2 \approx 1.1\times 10^3$ km s^{-1}, if we use the following observation data: $kT_1 \sim 6-7$ keV and $M_s \sim 1.3-1.5$ (van Weeren et al. 2016). Thus, setting $W \approx 1.3$, $u_{2,3} \approx 1.1$, and $t_{\rm age} \approx 110$ My, the width of low-frequency radio emission behind a *steady planar* shock becomes $\Delta l_{\rm low} \approx 120$ kpc. On the other hand,

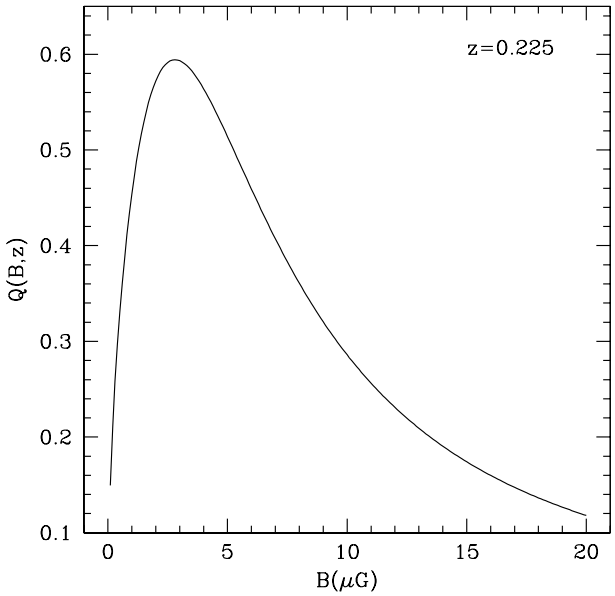

Figure 1. The factor $Q(B,z)$ for $z = 0.225$ given in Equation (7).

at high frequencies, for example, at $\nu_{\rm obs} = 630$ MHz it becomes only $\Delta l_{\rm high} \approx 78$ kpc for the largest value $Q_{\rm max} \approx 0.6$ (with $B \approx 2.8\ \mu$G).

As shown in Figure 2, the projected relic width of a spherical shell can be larger than $\Delta l_{\rm low}$ or $\Delta l_{\rm high}$, if the arc-like partial shell (marked in blue) is tilted with respect to the sky plane (dashed line). On the other hand, if the shell were to be viewed almost face-on, the spectral index α would be roughly constant across the width of the relic, which is in contradiction with observations (van Weeren et al. 2016). Later we will consider models with the various projection angles, $-5^\circ \le \psi_1 \le +15^\circ$ and $0^\circ \le \psi_2 \le +35^\circ$.

3. Numerical Calculations

The numerical setup and physical models for DSA simulations were described in detail in Kang (2015b). So only basic features are given here.

3.1. DSA Simulations for 1D Spherical Shocks

We follow time-dependent diffusion-convection equation for the pitch-angle-averaged phase space distribution function for CR electrons, $f_e(r,p,t) = g_e(r,p,t)p^{-4}$, in the one-dimensional (1D) spherically symmetric geometry:

$$\frac{\partial g_e}{\partial t} + u\frac{\partial g_e}{\partial r} = \frac{1}{3r^2}\frac{\partial(r^2u)}{\partial r}\left(\frac{\partial g_e}{\partial y} - 4g_e\right) + \frac{1}{r^2}\frac{\partial}{\partial r}\left[r^2 D(r,p)\frac{\partial g_e}{\partial r}\right] + p\frac{\partial}{\partial y}\left(\frac{b}{p^2}g_e\right), \quad (8)$$

where $u(r,t)$ is the flow velocity, $y = \ln(p/m_e c)$, m_e is the electron mass, and c is the speed of light (Skilling 1975). Here r is the radial distance from the center

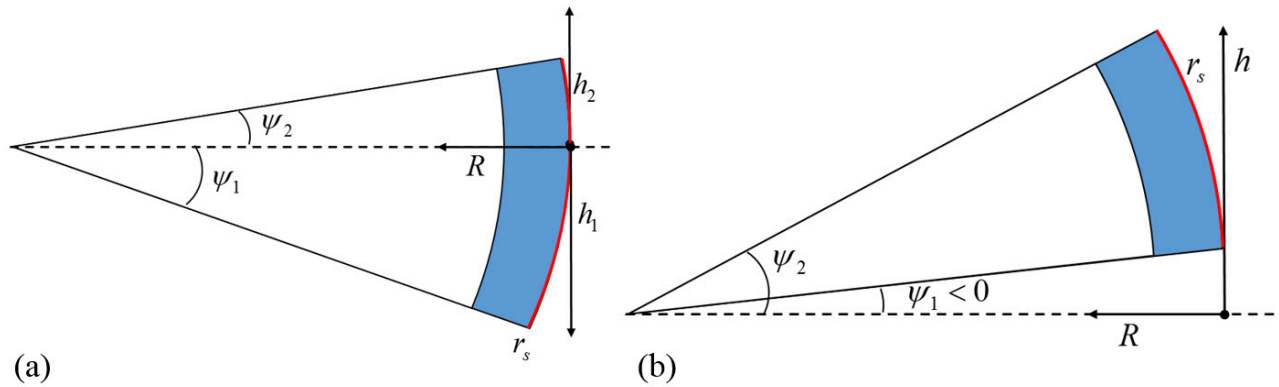

Figure 2. Two geometrical configurations of the radio-emitting volume (marked in blue) downstream of a spherical shock at r_s (marked in red) for the Toothbrush relic. The dashed line represents the plane of the sky, while the path lengths, h, h_1, and h_2 are parallel to lines of sights.

of the spherical coordinate, which assumed to coincide with the cluster center. We assume a Bohm-like spatial diffusion coefficient, $D(r,p) \propto p/B$. The cooling term $b(p) = -dp/dt = -p/t_{\rm rad}$ accounts for electron synchrotron and iC losses. The test-particle version of CRASH (Cosmic-Ray Amr SHock) code in a comoving 1D spherical grid is used to solve Equation (8) (Kang & Jones 2006).

3.2. Models for Magnetic Fields

We consider simple yet physically motivated models for the postshock magnetic fields as in Kang (2015b): (1) the magnetic field strength across the shock transition is assumed to increase due to compression of the two perpendicular components,

$$B_2(t) = B_1\sqrt{1/3 + 2\sigma(t)^2/3}, \tag{9}$$

where B_1 and B_2 are the preshock and postshock magnetic field strengths, respectively, and $\sigma(t) = \rho_2/\rho_1$ is the density compression ratio across the shock. (2) for the downstream region ($r < r_s$), the magnetic field strength is assumed to scale with the gas pressure:

$$B_{\rm dn}(r,t) = B_2(t) \cdot [P_g(r,t)/P_{g,2}(t)]^{1/2}, \tag{10}$$

where $P_{g,2}(t)$ is the gas pressure immediately behind the shock.

3.3. Preshock Electron Population

Several possible origins for pre-existing, relativistic electron populations in the ICMs can be considered: (1) old remnants of radio jets from AGNs (radio ghosts), (2) electron populations that were accelerated by previous shocks, and (3) electron populations that were accelerated by turbulence during merger activities (e.g., Kang & Ryu 2015). In the case of the Toothbrush relic, van Weeren et al. (2016) suggested that the AGN located at the southwestern end of B1 relic might be the candidate source that supplies relativistic plasmas to this relic.

Here we assume that a preshock population of electrons has a power-law spectrum with exponential cutoff as follows:

$$f_{\rm up}(p) \propto p^{-s} \exp\left[-\left(\frac{\gamma_e}{\gamma_{e,c}}\right)^2\right], \tag{11}$$

where $s = 4.6$ is chosen to match the observed shock index, $\alpha_{\rm sh} \approx 0.8$. We consider several models with a range of the cutoff Lorentz factor, $\gamma_{e,c} = 2 - 10 \times 10^4$, and find that $\gamma_{e,c} \sim 7-8\times10^4$ produces the best match to the observations of both Stroe et al. (2016) and van Weeren et al. (2016).

Note that this preshock electron population could be detected in radio, as can be seen in Figure 3, since $\gamma_{e,c}$ is quite high. However, no radio fluxes have been detected north of the northern edge of B1 (the shock location) (van Weeren et al. 2016). Since the candidate AGN is located about 200 kpc downstream of the shock location, it is possible that the shock has almost swept through the upstream region with these preshock electrons emitted by the AGN.

In order to isolate the effects of the pre-existing population, the *in situ* injection at the shock is turned off in the DSA simulations presented here.

3.4. Shock Parameters

The shock parameters are chosen to emulate roughly the shock associated with B1 relic in the Toothbrush cluster. According to van Weeren et al. (2016), $kT_1 = 8.3^{+3.2}_{-2.4}$ keV and $kT_2 = 8.2^{+0.7}_{-0.9}$ keV across B1, so the postshock temperature is better constrained, compared to the preshock temperature. Considering that $\Delta l_{\rm high}$ is smaller than the observed width ($\sim$ 110 kpc) at 610 MHz, we choose a higher value of $kT_2 = 8.9$ keV in order to maximize $\Delta l_{\rm high}$. Then we choose two values of the initial Mach number, which determine the preshock temperature and the initial shock speed as follows:

(1) $M_{s,i} = 1.3$, $kT_1 = 6.9$ keV, $u_{s,i} = 1.8 \times 10^3$ km s^{-1}, and $\gamma_{e,c} = 8 \times 10^4$.

(2) $M_{s,i} = 1.5$, $kT_1 = 5.9$ keV, $u_{s,i} = 1.9 \times 10^3$ km s^{-1},

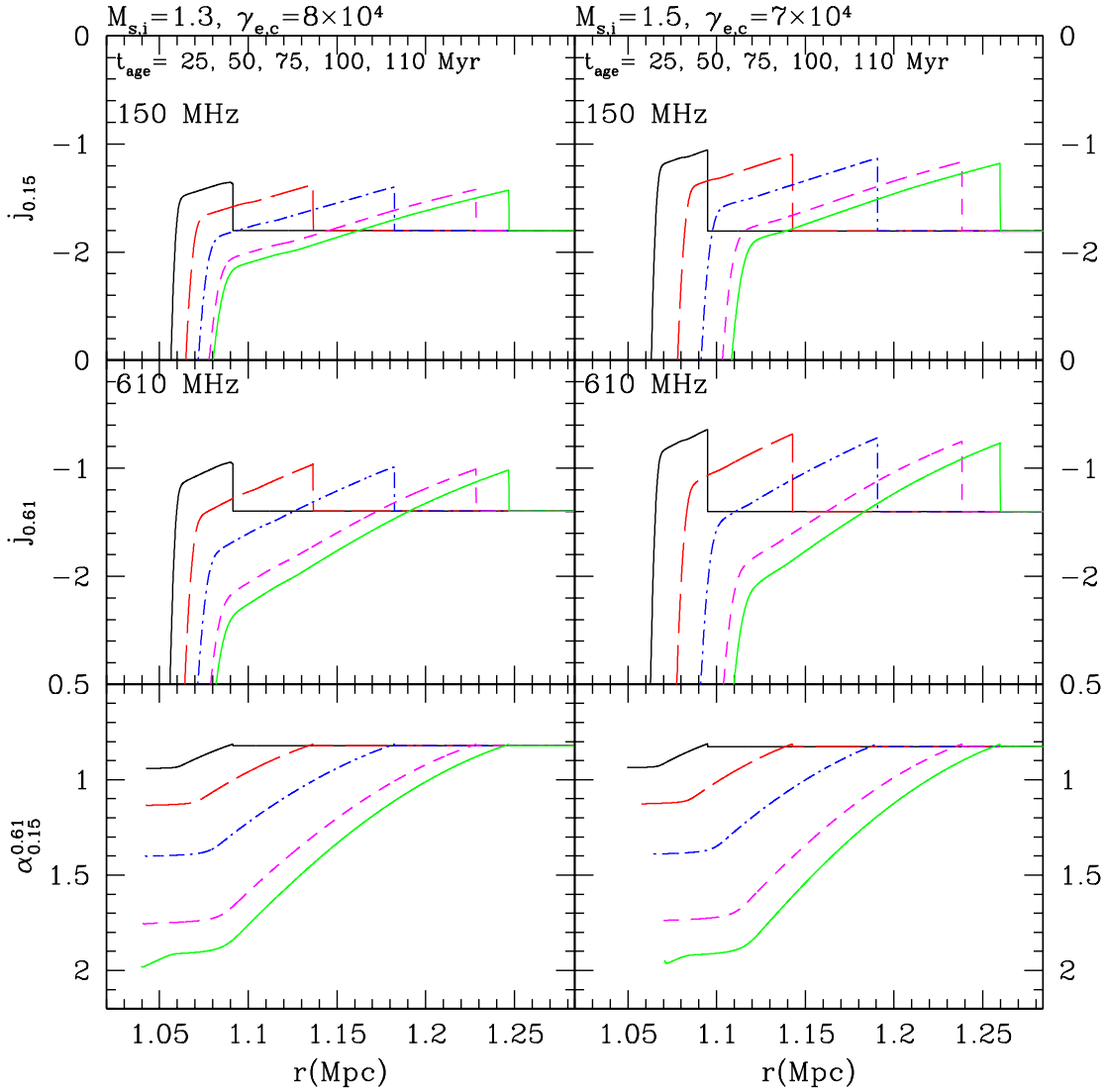

Figure 3. Time evolution of the synchrotron emissivity, $j_\nu(r)$ at 150 MHz (top panels) and 610 MHz (middle), and the spectral index, $\alpha_{0.15}^{0.61}$ between 150 and 610 MHz (bottom) plotted as a function of the radial distance from the cluster center, r(Mpc), in the two models with the initial Mach number $M_{s,i} = 1.3$ (left panels) and $M_{s,i} = 1.5$ (right panels). The results at 25 (black solid lines), 50 (red long dashed), 75 (blue dot-dashed), 100 (magenta dashed), and 110 Myr (green solid) are presented.

and $\gamma_{e,c} = 7 \times 10^4$.

The spherical shock slows down to $M_s \approx 1.2$ in the $M_{s,i} = 1.3$ model and to $M_s \approx 1.4$ in the $M_{s,i} = 1.5$ model at the shock age of $t_{\rm age} \approx 110$ Myr. The preshock magnetic field strength is assumed to be $B_1 = 2$ μG, resulting in the postshock strength, $B_2 = 2.5 - 2.8$ μG.

The density of the background gas in the cluster outskirts is assumed to decrease as $\rho_{\rm up} = \rho_0(r/r_{s,i})^{-2}$. This corresponds to the so-called beta model for isothermal ICMs, $\rho(r) \propto [1 + (r/r_c)^2]^{-3\beta/2}$ with $\beta \sim 2/3$ (Sarazin 1988).

4. Results of DSA Simulations

Figure 3 shows the synchrotron emissivity, $j_\nu(r)$ at 150 MHz and 610 MHz, and the spectral index, $\alpha_{0.15}^{0.61}$ between the two frequencies in the models with $M_{s,i} = 1.3$ and $M_{s,i} = 1.5$. It illustrates how the downstream radio-emitting region broadens in time as the spherical shock moves outward away from the cluster center, and how the radio spectrum steepens behind the shock further in time. In the model with $M_{s,i} = 1.3$, the emissivities at both frequencies increase by a factor of $2.4 - 2.7$ across the shock, while they increase by a factor of $4.3 - 5.6$ in the model with $M_{s,i} = 1.5$. Again note that no radio fluxes have been detected in the upstream region of B1 relic (van Weeren et al. 2016). In that regard, the $M_{s,i} = 1.5$ model might be preferred, since it has a larger amplification factor across the shock.

The emissivity $j_{0.61}(r)$ decreases much faster than $j_{0.15}(r)$ does behind the shock, since the cooling length of higher energy electrons is shorter than that of lower

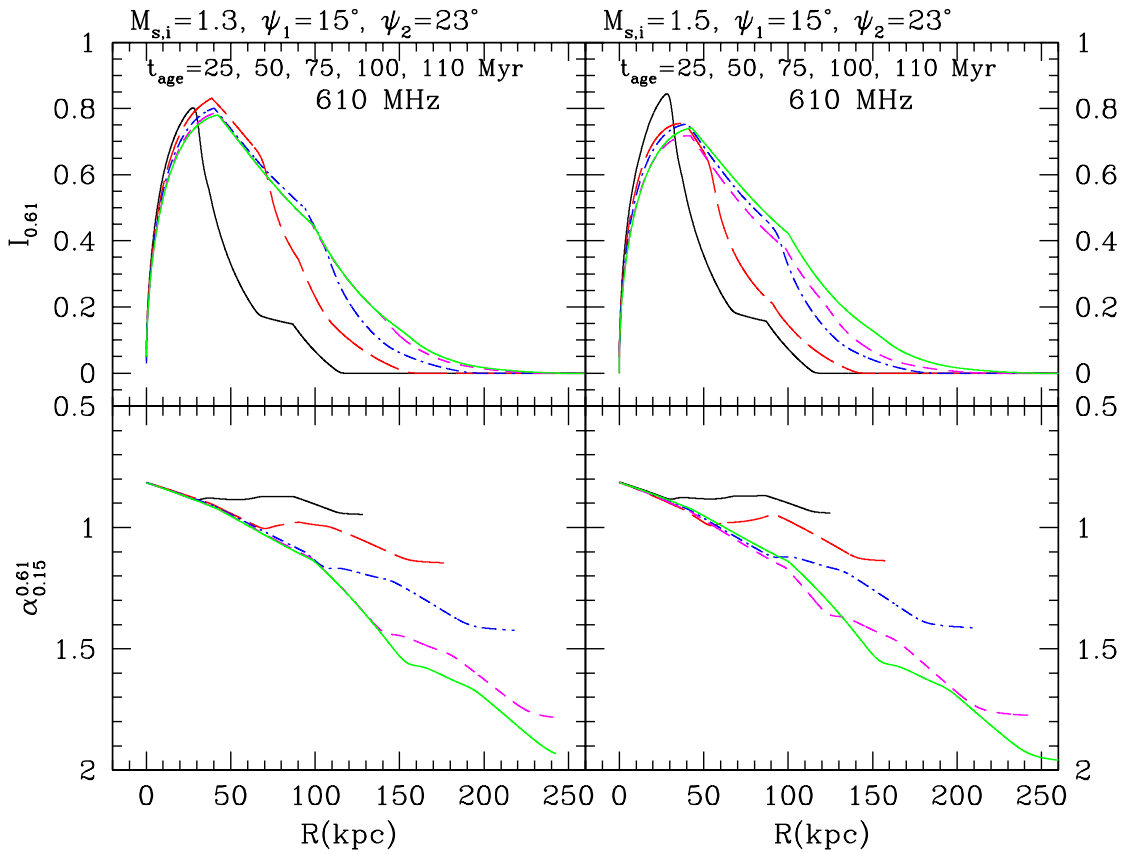

Figure 4. Time evolution of the surface brightness I_ν at 610 MHz in arbitrary units (top panels) and the spectral index, $\alpha_{0.15}^{0.61}$ between 150 and 610 MHz plotted as a function of the projected distance behind the shock, R(kpc), in the two models with the initial Mach number $M_{s,i} = 1.3$ (left panels) and $M_{s,i} = 1.5$ (right panels). The projection angles are assume to be $\psi_1 = 15°$ and $\psi_2 = 23°$. The results at 25 (black solid lines), 50 (red long dashed), 75 (blue dot-dashed), 100 (magenta dashed), and 110 Myr (green solid) are presented.

energy electrons. The spectral index at the shock is $\alpha_{0.15}^{0.61} \approx 0.8$, since the slope of the pre-existing electron population is $s = 4.6$ in Equation (11). It increases to $\alpha_{0.15}^{0.61} \approx 1.9$ at the far downstream regions, which is in good agreement with observations.

Note that in the shock rest frame the postshock flow speed, $u_{\rm dn}(r,t)$, increases behind a spherically expanding shock, while it is uniform behind a steady planar shock. As a result, at the shock age of 110 My, for instance, the advection length becomes ~ 160 kpc in the simulations, which is larger than $\Delta l_{\rm low} \approx 120$ kpc estimated for a planar shock in Equation (5).

4.1. Surface Brightness and Spectral Index Profiles

The radio surface brightness, $I_\nu(R)$, is calculated from the emissivity $j_\nu(r)$ by adopting the same geometric volume of radio-emitting electrons as in Figure 1 of Kang (2015b). Here R is the distance behind the projected shock edge in the plane of the sky, while r is the radial distance from the cluster center. As shown in Figure 2, various projection angles $\psi_1 + \psi_2 = 30° - 45°$ should be considered in order to explore projection effects. For example, if both $\psi_1 > 0$ and $\psi_2 > 0$, the surface brightness is calculated as follow:

$$I_\nu(R) = \int_0^{h_{1,\rm max}} j_\nu(r) dh_1 + \int_0^{h_{2,\rm max}} j_\nu(r) dh_2, \quad (12)$$

where h is the path length along line of sights. Note that the radio flux density, S_ν, can be obtained by convolving I_ν with a telescope beam as $S_\nu(R) \approx I_\nu(R)\pi\theta_1\theta_2(1+z)^{-3}$, if the brightness distribution is broad compared to the beam size of $\theta_1\theta_2$. In addition, the spectral index, $\alpha_{0.15}^{0.61}$ is calculated from the projected $I_\nu(R)$ at 150 and 610 MHz.

Figure 4 shows how $I_\nu(R)$ at 610 MHz and $\alpha_{0.15}^{0.61}$ evolve during 110 Myr in the two shock models. The projection angles, $\psi_1 = 15°$ and $\psi_2 = 23°$, are chosen to match the observed profiles of $I_\nu(R)$ and $\alpha_{0.15}^{0.61}$, as shown in Figure 5. The shock has weakened to $M_s \approx 1.2$ in the $M_{s,i} = 1.3$ model and $M_s \approx 1.4$ in the $M_{s,i} = 1.5$ model at 110 Myr. In the early stage the relic width increases roughly with time. But in time it asymptotes to the cooling lengths, since the cooling of high energy electrons begins to control the width at later time.

The gradient of $\alpha_{0.15}^{0.61}$ increases in time as postshock

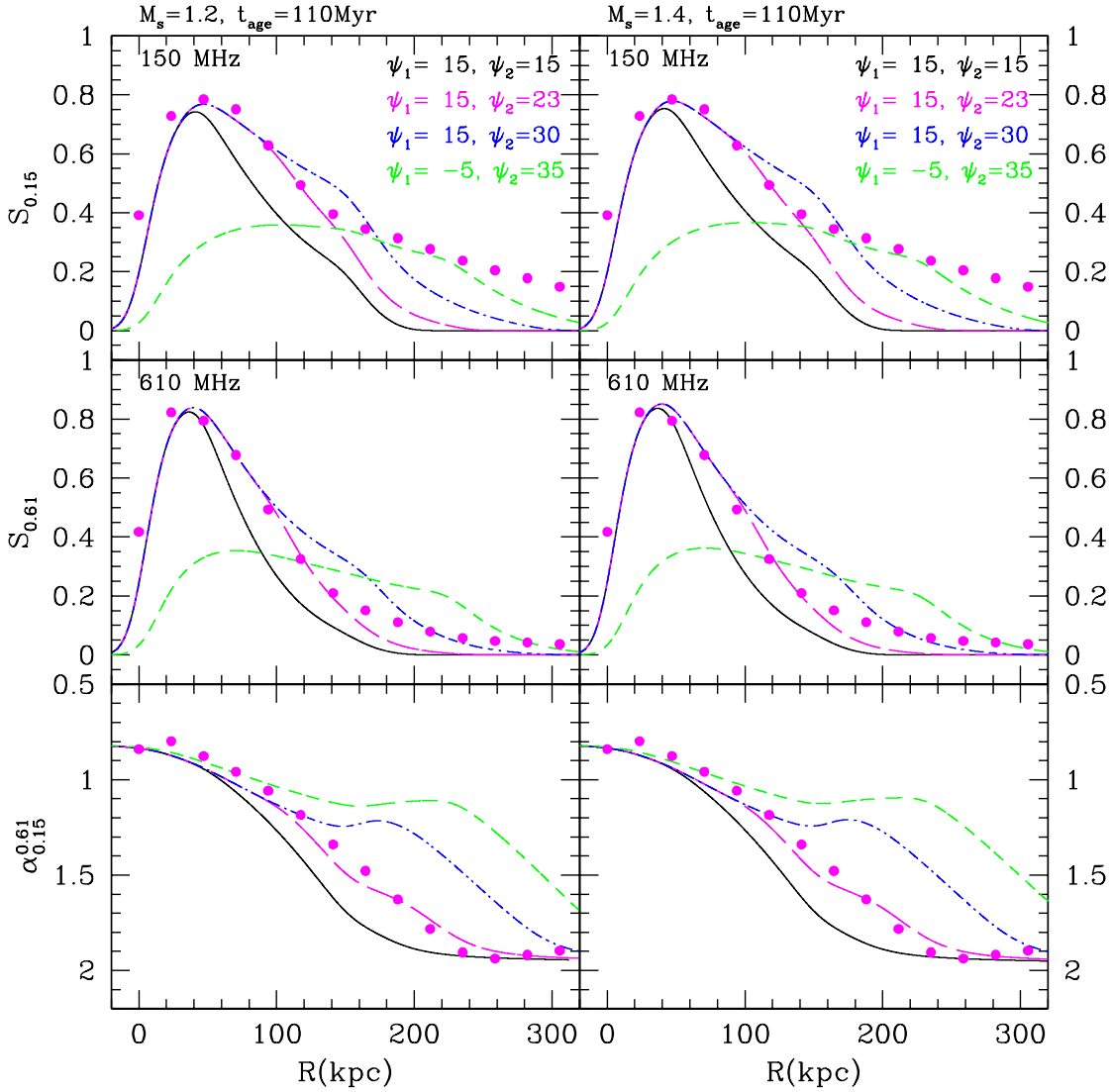

Figure 5. Radio flux density S_ν at 150 MHz (top panels) and at 610 MHz (middle panels) in arbitrary units, and the spectral index $\alpha_{0.15}^{0.61}$ between the two frequencies (bottom panels) plotted as a function of projected distance behind the shock, R(kpc), for the shock models with $M_s = 1.2$ (left panels) and $M_s = 1.4$ (right panels) at $t_{\rm age} = 110$ Myr . The projection angles, ψ_1 and ψ_2, for different curves are given in the plot. Gaussian smoothing with 6.5″ resolution (≈ 23.5 kpc) is applied in order to emulate radio observations. The magenta dots are the observational data of van Weeren et al. (2016).

electrons lose energies. At $t_{\rm age} = 110$ My (green solid lines), the spectral index increases from $\alpha_{0.15}^{0.61} \approx 0.8$ at the shock location to $\alpha_{0.15}^{0.61} \approx 1.9$ about 230 kpc downstream of the shock in the two models. Note that the evolution of $\alpha_{0.15}^{0.61}$ depends on the cutoff energy of the pre-existing electron populations. In order to obtain the observed profile that steepens from 0.8 to 1.9 over 230 kpc, we should choose $\gamma_{e,c} \approx 8 \times 10^4$ for $M_{s,i} = 1.3$ model and $\gamma_{e,c} \approx 7 \times 10^4$ for $M_{s,i} = 1.5$ model.

We find that the best fits to the observations of van Weeren et al. (2016) (magenta dots) are obtained at 110 Myr for both models. Figure 5 shows the radio flux density $S_\nu(R)$ at 150 and 610 MHz and $\alpha_{0.15}^{0.61}$ at $t_{\rm age} = 110$ Myr for different sets of ψ_1 and ψ_2. Note that Gaussian smoothing with 6.5″ resolution (≈ 23.5 kpc) is applied in order to emulate radio observations. The scales of $S_\nu(R)$ are rescaled in arbitrary units. If we were to attempt to match the observed profile of $S_{0.15}$ up to $\sim$ 300 kpc, then one of the projection angles should be larger than 35° (green dashed lines), as can be seen in the top panels. With such projection angles, however, the predicted profile of $\alpha_{0.15}^{0.61}$ would be much flatter than the observed profile. Since the observed radio fluxes could be contaminated by the halo components, we try to fit the observed profiles only for $R < 150$ kpc. As can be seen in the figure, the model with $\psi_1 = 15°$ and $\psi_2 = 23°$ (magenta long dashed lines) gives the best match to the observations. At 110 Myr the shock radius is $r_s(t) \approx 1.25 - 1.26$ Mpc (see Figure 3). Note that in fitting the profile of $S_\nu(R)$ with $\psi_1 = 15°$ and $\psi_2 = 23°$, $r_s(t)(1 - \cos\psi_1) \approx 43$ kpc is matched with the peak position at $\sim$ 47 kpc, while

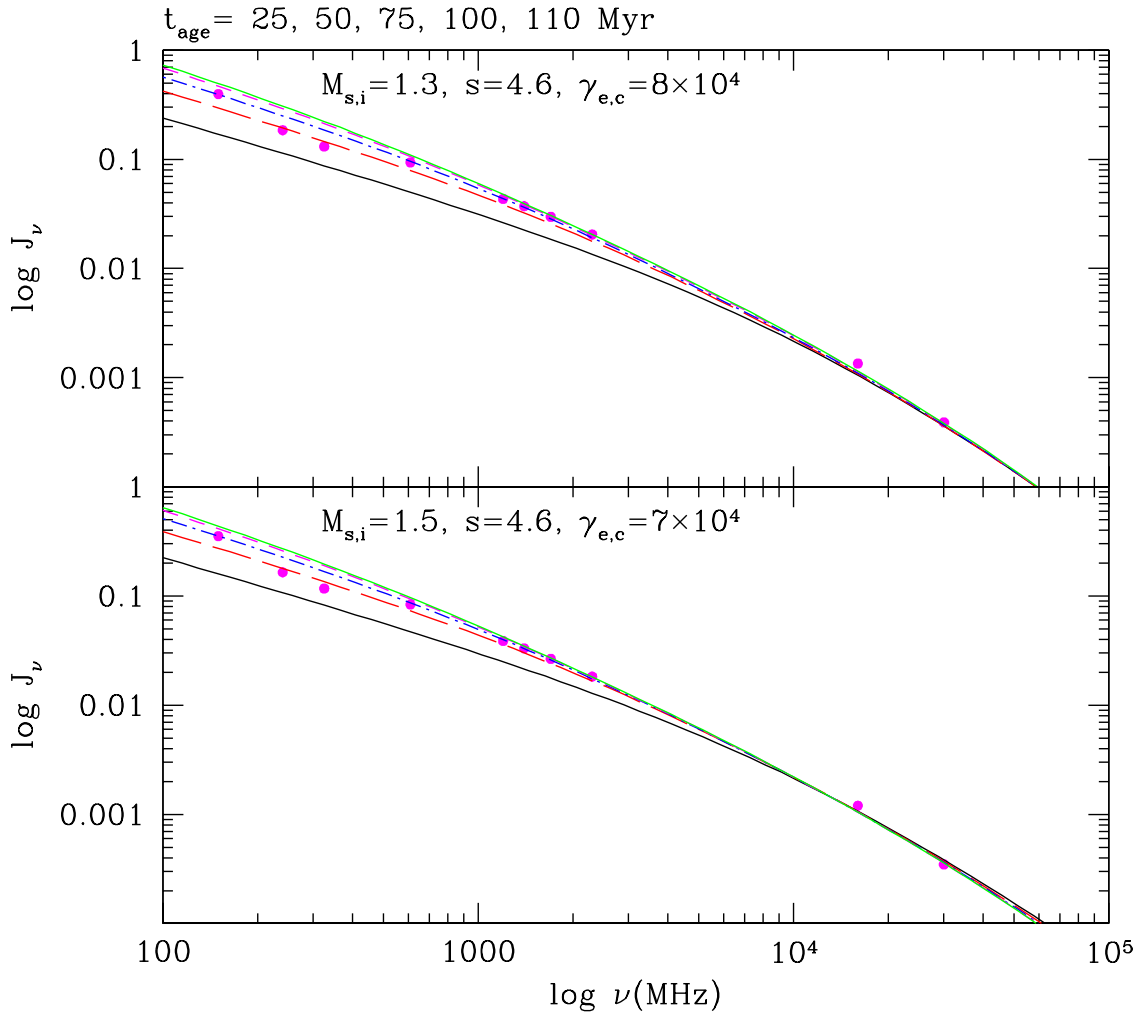

Figure 6. Time evolution of volume-integrated radio spectrum for the shock models with $M_{s,i} = 1.3$ (top panels) and $M_{s,i} = 1.5$ (bottom) at $t_{\rm age} = 25$ (black solid lines), 50 (red long-dashed), 75 (blue dot-dashed), 100 (magenta dashed), and 110 Myr (green solid). The magenta dots are the observational data taken from Table 3 of Stroe et al. (2016).

$r_s(1-\cos\psi_2) \approx 100$ kpc is matched with the relic width of $\sim 110 - 140$ kpc.

4.2. Integrated Spectrum

As described in Section 2.1, the volume integrated radiation spectrum of a typical cluster shock with $t_{\rm age} \sim 100$ Myr is expected to steepen from $\alpha_{\rm sh}$ to $\alpha_{\rm sh} + 0.5$ gradually over $0.1 - 10$ GHz. In the re-acceleration model, however, it also depends on the spectral shape of the preshock electron population. So the spectral curvature of the observed spectrum can be reproduced by adjusting the set of model parameters, i.e., M_s, B_1, $t_{\rm age}$, s and $\gamma_{e,c}$ in our models.

Figure 6 shows the time evolution of the integrated spectrum, J_ν, during 110 Myr in the two shock models. The magenta dots show the observational data taken from Table 3 of Stroe et al. (2016), which are rescaled to fit the simulated spectrum near 1 GHz by eye. We find that $\gamma_{e,c} = 7 - 8 \times 10^4$ is needed in order to reproduce J_ν both near 1 GHz and $16 - 30$ GHz simultaneously. At 110 Myr (green solid lines) the predicted fluxes are slightly higher than the observed fluxes for $0.1 - 1$ GHz, while the predicted fluxes are in good agreement with the observed fluxes for $1 - 30$ GHz. We can conclude that the model spectra agree reasonably well with the observed spectrum of B1 relic reported by Stroe et al. (2016).

5. SUMMARY

We have performed time-dependent, DSA simulations of one-dimensional, spherical shocks, which sweep through the ICM thermal plasma with a population of relativistic electrons ejected from an AGN. In order to reproduce the observational data for B1 (head portion) of the Toothbrush relic (van Weeren et al. 2016), we adopt the following parameters: $kT_1 \approx 5.9 - 6.9$ keV, $M_{s,i} = 1.3 - 1.5$, $u_{s,i} = 1.8 - 1.9 \times 10^3$ km s^{-1}, and $B_1 = 2\ \mu$G.

In addition, we assume that the preshock gas contains a pre-existing electron population of a power-law

spectrum with the slope $s = 4.6$ and exponential cutoff at $\gamma_{e,c} = 7 - 8 \times 10^4$ as given in Equation (11). The power-law slope s is chosen to match the observed radio spectral index, $\alpha_{\rm sh} \approx 0.8$, while $\gamma_{e,c}$ is adjusted to match both observed spectral aging measured by the spatial gradient of $\alpha_{0.15}^{0.61}$ and spectral curvatures in the integrated radio spectrum of B1 relic for $1 - 30$ GHz (Stroe et al. 2016).

Note that the preshock region could be radio-luminous with the pre-existing electrons with such high energies. In the DSA models considered here, the synchrotron emissivity increases across the shock by a factor of $2.4 - 2.7$ in the $M_{s,i} = 1.3$ model and by a factor of $4.3 - 5.6$ in the $M_{s,i} = 1.5$ model. Considering that the candidate source AGN is located about 200 kpc downstream of the shock (the northern edge of B1 relic) and there is no detectable radio fluxes in the preshock region, we suspect that the shock might have swept through the region permeated by relativistic plasma ejected from the source AGN.

After 110 Myr, the spherical shock slows down to $M_s \approx 1.2 - 1.4$ with the postshock magnetic field strength $B_2 \approx 2.5 - 2.8$ μG. At this stage, we find that the spatial profiles of the radio flux density, S_ν, and the radio spectral index, $\alpha_{0.15}^{0.61}$, and the integrated radio spectrum, J_ν, become consistent with the observations of B1 relic (van Weeren et al. 2016; Stroe et al. 2016).

The advection length behind the spherically expanding shock is greater than that estimated for a planar shock in Equation (5), because the postshock flow speed in the shock rest frame increases downstream away from the shock. Moreover, the width of the projected surface brightness of a spherical shell depends on the projection angles as shown in Figure 2. In fact, the observed profiles of radio fluxes at 150 MHz and 610 MHz can be modeled with the projection angles, $\psi_1 = 15°$ and $\psi_2 = 23°$ for the shock model at $t_{\rm age} \approx 110$ Myr, as shown in Figure 5. So the arc-like radio-emitting shell is likely to be tilted slightly with respect to the sky plane as shown in the case (a) of Figure 2.

This study demonstrates that the re-acceleration of pre-existing relativistic electrons could explain the discrepancy between the radio spectral index and the shock Mach number inferred from X-ray observations that has been found in some radio relics such as the Toothbrush relic (Akamatsu & Kawahara 2013) and the Sausage relic (Stroe et al. 2016). Considering the ubiquitous presence of radio galaxies and presumed radio ghosts in the ICM, the low acceleration efficiency of weak shocks, and the relative rarity of radio relics compared to the expected occurrence of merger-induced shocks, we suggest that at least for the radio relics with $M_{\rm radio} > M_{\rm X}$, the re-acceleration model is preferred to the *in situ* injection model.

Acknowledgments

This research was supported by Basic Science Research Program through the National Research Foundation of Korea (NRF) funded by the Ministry of Education (2014R1A1A2057940). The author thanks R. J. van Weeren for providing the radio flux data for the Toothbrush relic published in van Weeren et al. (2016).

References

Akamatsu, H., & Kawahara, H. 2013, Systematic X-Ray Analysis of Radio Relic Clusters with Suzaku, PASJ, 65, 16

Brüggen, M., Bykov, A., Ryu, D., & Röttgering, H. 2012, Magnetic Fields, Relativistic Particles, and Shock Waves in Cluster Outskirts, Space Sci. Rev., 166, 187

Brunetti, G., & Jones, T. W. 2014, Cosmic Rays in Galaxy Clusters and Their Nonthermal Emission, Int. J. Mod. Phys. D, 23, 30007

Clarke, T. E., Randall S. W., Sarazin, C. L., et al. 2013, Chandra View of the Ultra-Steep Spectrum Radio Source in A2443: Merger Shock-Induced Compression of Fossil Radio Plasma?, ApJ, 772, 84

de Gasperin, F., Ogrean, G. A., van Weeren, R. J., et al. 2015, Abell 1033: Birth of a Radio Phoenix, MNRAS, 448, 2197

Drury, L. O'C. 1983, An Introduction to the Theory of Diffusive Shock Acceleration of Energetic Particles in Tenuous Plasmas, Rept. Prog. Phys., 46, 973

Ensslin, T. A. 1999, Radio Ghosts, in Ringberg Workshop on Diffuse Thermal and Relativistic Plasma in Galaxy Clusters, ed. P. S. H. Böhringer, L. Feretti, MPE Report 271, 275

Ensslin, T. A., Biermann, P. L., Kleing, U., & Kohle, S. 1998, Cluster Radio Relics as a Tracer of Shock Waves of the Large-Scale Structure Formation, A&A, 332, 395

Ensslin, T. A., & Brüggen, M. 2002, On the Formation of Cluster Radio Relics, MNRAS, 331, 1011

Ensslin, T. A., & Gopal-Krishna. 2001, Reviving Fossil Radio Plasma in Clusters of Galaxies by Adiabatic Compression in Environmental Shock Waves, A&A, 366, 26

Feretti, L., Giovannini, G., Govoni, F., & Murgia, M. 2012, Clusters of Galaxies: Observational Properties of the Diffuse Radio Emission, A&A Rev., 20, 54

Hong, E. W., Ryu, D., Kang, H., & Cen, R. 2014, Shock Waves and Cosmic Ray Acceleration in the Outskirts of Galaxy Clusters, ApJ, 785, 133

Itahana, M., Takizawa, M., Akamatsu, H., et al. 2015, Suzaku Observations of the Galaxy Cluster 1RXS J0603.3+4214: Implications of Particle Acceleration Processes in the "Toothbrush" Radio Relic, PASJ, 67, 113

Kang, H. 2011, Energy Spectrum of Nonthermal Electrons Accelerated at a Plane Shock, JKAS, 44, 49

Kang, H. 2015a, Nonthermal Radiation from Relativistic Electrons Accelerated at Spherically Expanding Shocks, JKAS, 48, 9

Kang, H. 2015b, Radio Emission from Weak Spherical Shocks in the Outskirts of Galaxy Clusters, JKAS, 48, 155

Kang, H., & Jones, T. W. 2006, Numerical Studies of Diffusive Shock Acceleration at Spherical Shocks, Astropart. Phys., 25, 246

Kang, H., & Ryu, D. 2011, Re-Acceleration of Non-Thermal Particles at Weak Cosmological Shock Waves, ApJ, 764, 95

Kang, H., & Ryu, D. 2015, Curved Radio Spectra of Weak Cluster Shocks, ApJ, 809, 186

Kang, H., & Ryu, D. 2016, Re-Acceleration Model for Radio Relics with Spectral Curvature, ApJ, 823, 13

Kang, H., Ryu, D., & Jones, T. W. 2012, Diffusive Shock Acceleration Simulations of Radio Relics, ApJ, 756, 97

Kang, H., Vahe, P., Ryu, D., & Jones, T. W. 2014, Injection of κ-like Suprathermal Particles into Diffusive Shock Acceleration, ApJ, 788, 141

Kempner, J. C., Blanton, E. L., Clarke, T. E., et al. 2004, Conference Note: A Taxonomy of Extended Radio Sources in Clusters of Galaxies, in The Riddle of Cooling Flows in Galaxies and Clusters of galaxies, ed. T. Reiprich, J. Kempner, & N. Soker, 335

Ogrean, G. A., Brüggen, M., van Weeren, R., Röttgering, H., Croston, J. H., & Hoeft, M. 2013, Challenges to Our Understanding of Radio Relics: X-Ray Observations of the Toothbrush Cluster, MNRAS, 433, 812

Pinzke, A., Oh, S. P., & Pfrommer, C. 2013, Giant Radio Relics in Galaxy Clusters: Re-Acceleration of Fossil Relativistic Electrons?, MNRAS, 435, 1061

Russell, H. R., van Weeren, R. J., Edge, A. C., et al. 2011 A Merger Mystery: No Extended Radio Emission in the Merging Cluster Abell 2146, MNRAS, 417, L1

Ryu, D., Kang, H., Hallman, E., & Jones, T. W. 2003, Cosmological Shock Waves and Their Role in the Large-Scale Structure of the Universe, ApJ, 593, 599

Sarazin, C. L. 1988, X-Ray Emission from Clusters of Galaxies (Cambridge: Cambridge University Press)

Shimwell, T. W., Markevitch, M., Brown, S., Feretti, L, et al., 2015, Another Shock for the Bullet Cluster, and the Source of Seed Electrons for Radio Relics, MNRAS, 449, 1486

Skilling, J. 1975, Cosmic Ray Streaming. I - Effect of Alfvén Waves on Particles, MNRAS, 172, 557

Skillman, S. W., Hallman, E. J., O'Shea, W., Burns, J. O., Smith, B. D., & Turk, M. J. 2011, Galaxy Cluster Radio Relics in Adaptive Mesh Refinement Cosmological Simulations: Relic Properties and Scaling Relationships, ApJ, 735, 96

Slee, O. B., Roy, A. L., Murgia, M., Andernach, H., & Ehle, M. 2001, Four Extreme Relic Radio Sources in Clusters of Galaxies, AJ, 122, 1172

Stroe, A., Shimwell, T. W., Rumsey, et al. 2016, The Widest Frequency Radio Relic Spectra: Observations from 150 MHz to 30 GHz, MNRAS, 455, 2402

Trasatti, M., Akamatsu, H., Lovisari, L., Klein, U., Bonafede, A., Brggen, M., Dallacasa, D., & Clarke, T. 2015, The Radio Relic in Abell 2256: Overall Spectrum and Implications for Electron Acceleration, A&A, 575, A45

van Weeren, R., Brunetti, G., Brüggen, M., et al. 2016, LOFAR, VLA, and CHANDRA Observations of the Toothbrush Galaxy Cluster, ApJ, 818, 204

van Weeren, R., Röttgering, H. J. A., Brüggen, M., & Hoeft, M. 2010, Particle Acceleration on Megaparsec Scales in a Merging Galaxy Cluster, Science, 330, 347

van Weeren, R. J., Röttgering, H. J. A., & Brüggen, M. 2011b, Diffuse Steep-Spectrum Sources from the 74 MHz VLSS Survey, A&A, 527, A114

van Weeren, R., Röttgering, H. J. A., Intema, H. T., Rudnick, L., Brüggen, M., Hoeft, M., & Oonk, J. B. R. 2012, The "Toothbrush-Relic": Evidence for a Coherent Linear 2-Mpc Scale Shock Wave in a Massive Merging Galaxy Cluster?, A&A, 546, 124

Vazza, F., Brunetti, G., & Gheller, C. 2009, Shock Waves in Eulerian Cosmological Simulations: Main Properties and Acceleration of Cosmic Rays, MNRAS, 395, 1333